Aerothermal Analysis of Film Cooling Flows

Katharina Stichling, Hans-Jörg Bauer
katharina.stichling@kit.edu

Institute of Thermal Turbomachinery (ITS)
Karlsruhe Institute of Technology (KIT)
Karlsruhe, Baden-Württemberg
Germany

Abstract

Flow field and thermal film cooling parameters are analysed and compared for different blowing ratios for a 10°-10°-10° laidback fan-shaped film cooling hole geometry with an inclination angle of 35° and a wide spacing of $^{P}/_{D} = 8$ to ensure the absence of jet interaction. The influence of the coolant ejection on the aerodynamics of the hot gas is investigated and stationary as well as non-stationary vortex structures are identified. The present study uses an existing test rig at the Institute of Thermal Turbomachinery (ITS) at the Karlsruhe Institute of Technology (KIT) designed for generic film cooling studies with high spatial resolution applying stereoscopic particle image velocimetry (SPIV) as well as infrared thermography (IRT). Operating conditions of hot gas and cooling air inlet and exit are uniquely compliant with scaled engine-realistic conditions, including temperature ratio, turbulence intensity and coolant flow configuration.

Keywords: turbine film cooling; heat transfer; infrared thermography; particle image velocimetry

NOMENCLATURE

Symbol	Unit	Description
Latin symbols		
h_f, h_0	$\mathrm{W/(m^2\,K)}$	heat transfer coefficient with and without film cooling
u, v, w	m/s	velocity in streamwise, lateral and wall-normal direction
$\dot{q}$	$\mathrm{W/m^2}$	heat flux
D	mm	film cooling hole diameter
L	mm	length
P	mm	hole pitch
T	K	temperature
Greek symbols		
$\eta_\mathrm{a,W}$	-	adiabatic film cooling effectiveness
δ	mm	boundary layer thickness
μ	kg s/m	dynamic viscosity
ν	$\mathrm{m^2/s}$	kinematic viscosity
θ, γ	°	camera angle, Scheimpflug angle
$\mathbf{\Phi}$	-	POD spatial modes
Indices		
$\square_\mathrm{abs}$		absolute quantity
$\square_\mathrm{c}$		referring to flow in cooling hole
$\square_\mathrm{cc}$		referring to flow in the coolant channel
$\square_\mathrm{h}$		referring to flow in hot gas channel
$\square_\mathrm{ref}$		reference value
$\square_\mathrm{t}$		total
Abbreviations		
CVP		counter-rotating vortex pair
FOV		field of view
IRT		infrared thermography
JICF		jet in cross-flow
LES		large eddy simulation
LFH		laidback fan-shaped hole
RANS		Reynolds averaged Navier Stokes
SPIV		stereoscopic particle image velocimetry

1.0 INTRODUCTION

To facilitate the development of even more efficient and sustainable gas turbines and aero-engines, increasing turbine entry temperatures have to be compensated by improved cooling methods, especially film cooling. Investigating influencing parameters such as blowing ratio ($\mathrm{BR} = {}^{(\rho u)_\mathrm{c}}/_{(\rho u)_\mathrm{h}}$), density ratio ($\mathrm{DR} = {}^{\rho_\mathrm{c}}/_{\rho_\mathrm{h}}$), velocity ratio ($\mathrm{VR} = {}^{(u)_\mathrm{c}}/_{(u)_\mathrm{h}}$) or momentum ratio ($\mathrm{IR} = {}^{(\rho u^2)_\mathrm{c}}/_{(\rho u^2)_\mathrm{h}}$), numerous experimental studies have been conducted with focus on determining the film cooling effectiveness $\eta_\mathrm{a,W}$ and in some cases also the ratio of heat transfer coefficients with and without film cooling ${}^{h_\mathrm{f}}/_{h_0}$.

The high cost of experimental investigations has encouraged putting more effort into conducting numerical studies. Due to the complex flow field, Reynolds averaged Navier Stokes (RANS) simulations are often insufficient to reliably predict locally resolved and sometimes even laterally averaged values of $\eta_\mathrm{a,W}$ when compared to experimental studies, even though turbulence models are often built specifically for film cooling applications [3]. Large eddy simulations (LES) are known to produce more reliable results [11, 25, 30], but the choice of sub-grid-scale model and turbulent inflow condition can have a strong impact on results and so far, there are no experimental investigations for film cooling realistic

operating conditions to validate the complex flow field in and around the film cooling hole to further improve modelling in numerical simulations [24].

Hence, extensive flow field measurements are required to improve the understanding of mixing between hot gas and coolant and the respective dominating steady and unsteady vortical structures. So far, very few studies present flow field measurements, most of which discuss time-averaged and only two-dimensional data. [21] investigated the effect of DR at different blowing ratios on the streamwise wall-normal centerplane using laser Doppler velocimetry. On comparing denser to unit-density jets, they found the velocity field of the former to vary significantly from the unit-density case. A description of four different vortical structures, namely, the jet shear layer vortices, a system of horseshoe vortices, the counter-rotating vortex pair and wake vortices was delivered mainly by means of flow visualization using smoke streaklines and smoke-filled jets by [9]. According to [10], an increase in turbulence intensity of the hot gas can be directly translated to an increase in lateral jet spreading for low blowing ratios.

[2] studied the three-dimensional time-averaged velocity field for cylindrical holes fed by a plenum. [28, 29] investigated the effect of freestream turbulence intensity on film cooling ejection at low blowing ratios and unity DR using two-dimensional particle image velocimetry (PIV) for cylindrical and fan-shaped holes, respectively. Similarly, the effects of DR on cylindrical holes using 2D PIV employed at the streamwise wall-normal centerplane were studied [12], showing a reduction of film cooling jet detachment towards elevated DRs. [6] conducted two-dimensional PIV of the streamwise wall-normal centerplane at low and high DRs. They presented snapshots of vorticity contours indicating the shear layer for different parameter configurations but at nearly zero free stream turbulence intensity, the operating parameters are far from realistic.

The more generic jet in crossflow configuration has been studied extensively in the past [16, 13]. Coolant crossflow at the hole inlet was considered in none of the previously mentioned studies and only [2] applied density ratios close to real-engine conditions. The three-dimensional flow field around an exiting film cooling jet in hot gas, though, clearly contains three-dimensional and transient flow phenomena [17]. These are highly dependent on parameters like DR, freestream turbulence intensity, and coolant flow supply configuration. Therefore, stereoscopic PIV measurements are of interest in particular due to their ability of capturing instantaneous three-dimensional velocity information. Experimental investigations providing the thermal film cooling parameters are further required optimally from the same test facility to be able to fully connect all aerothermal effects. Aside from improving the understanding of the flow field and heat transfer phenomena, such data can be valuable for the validation and further improvement of numerical models and simulation tools.

2.0 EXPERIMENTAL SETUP

In the following sections, an overview of the test facility, the measurement setup and the measurement principles is provided. Furthermore, measurement uncertainties are discussed.

2.1 Test section and measurement setup

Schematics of the test section and measurement setup are displayed in Figure 1. The velocity and temperature field uniformity of the inlet hot gas flow of the test section in Figure 1a has been validated [7] in previous works. The hot gas and coolant channel can be oriented either in parallel or perpendicular to each other, which facilitates realistic inflow conditions present in gas turbines and aero engines. In Table 2, the operating conditions for this study, which are derived from real-engine conditions, are listed.

A turbulence grid [22] ① and a subsequent boundary layer bleed ② are used to ensure well-defined and engine-like flow conditions at the coolant ejection. The interchangeable ejection module ③ connects the coolant and hot gas channel containing five separate film cooling holes aligned laterally at a constant x/D-position. A hot gas channel width of $50D$ prevents any interaction between the coolant jets and channel side walls. To minimise temperature change of the coolant during ejection, a low thermal conductivity is required. The ejection module is, hence, manufactured from polyetheretherketone (PEEK), a semi-crystalline high-temperature-resistant thermoplastic ($\lambda_{\mathrm{th}} \approx 0.27\,\mathrm{W/(m\,K)}$). Optical access through the top wall of the hot gas channel for temperature field acquisition on the thermal measurement plate ⑤ is provided by five infrared-transmissive sapphire windows ④ using a camera sensitive for infrared radiation between 3...5 μm ⑥. A routine for temperature calibration of high-dynamic-range temperature data developed at ITS was used for data evaluation [18, 19]. The thermal

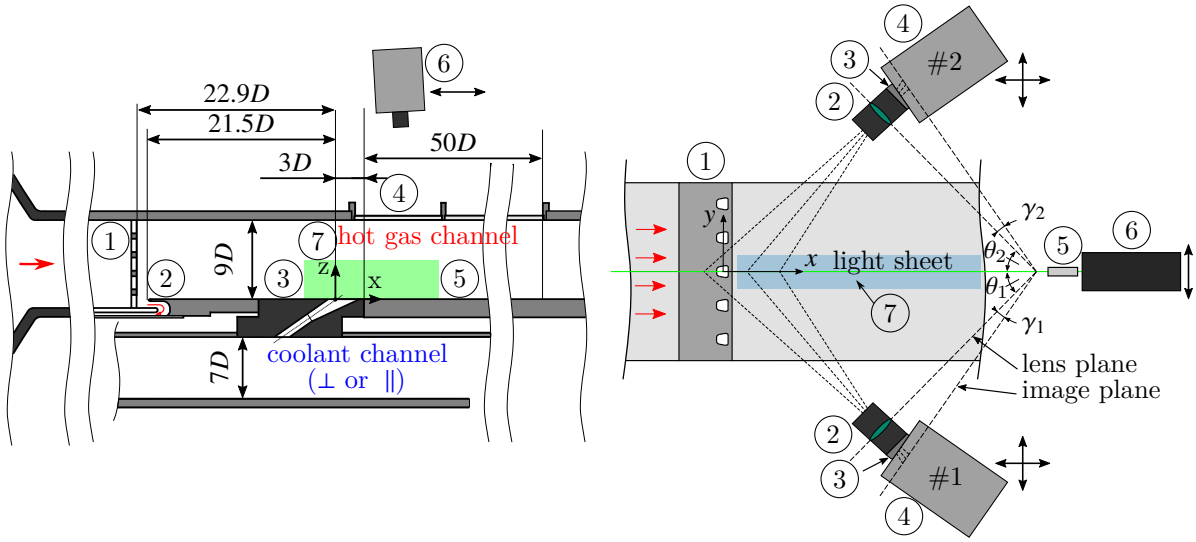

(a) Test section schematic with hot gas and coolant channel including a turbulence grid ①, boundary layer suction ②, ejection module ③, optical access for IRT ④, thermal measurement plate ⑤, IRT camera ⑥ and FOV for SPIV ⑦; adapted from [7]

(b) Schematic SPIV setup as top view on test section including: ejection module ①, camera lens ②, Scheimpflug adapter ③, camera ④, light sheet optics ⑤, ND:YLF laser ⑥ and FOV for IRT ⑦; adapted from [23]

Figure 1: Schematics of test section and measurement setup including FOVs for IRT and SPIV measurements

film cooling quantities were calculated using the superposition principle of film cooling [5], which is why two different measurement plates are used. Details of the calculation of the film cooling quantities can be found in [7].

The test section was originally constructed for the acquisition of adiabatic film cooling effectiveness $\eta_{a,W}$ and the ratio of heat transfer coefficients with and without film cooling h_f/h_0 [7, 8] only, and was later adapted to accommodate stereoscopic particle image velocimetry (SPIV) measurements [23]. The field of view (FOV) ⑦ is indicated by the green area in Figure 1a and is in fact comprised of two separate measurement planes with a slight overlap in streamwise direction to ensure a high spatial measurement resolution. The SPIV measurement setup is sketched in Figure 1b using a top view on the hot gas channel of the test section from Figure 1a. For the SPIV measurement, optical access is granted via two fused silica windows (not displayed), one on each lateral wall of the hot gas channel.

The light sheet with a thickness of $\delta_z \approx 1.5\,\text{mm}$ is generated using a green ($\lambda = 527\,\text{nm}$) dual pulse ND:YLF laser ⑥ (Darwin-Duo by Quantronix) and a light sheet optics ⑤. The cameras ④ (Fastcam SA5 CMOS cameras by Photron, max. pixel resolution 1.024 px × 512 px) are each used in conjunction with a 200 mm focal length lens ② connected via a Scheimpflug adapter ③. The Scheimpflug angle γ subtended by lens and image plane is adjusted to meet the Scheimpflug criterion to compensate for the

Table 2: Operating parameters of the test section

Parameter	Variable	Value
Reynolds number hot gas	$Re_{D,h}$	13×10^3
Reynolds number coolant	$Re_{D,cc}$	30×10^3
Density ratio	DR	1.7
Turbulence intensity hot gas	Tu_h	8.2 %
Blowing ratio	BR	1.0...3.0
Velocity ratio	u_{cc}/u_h	≈ 0.15
Total temperature hot gas	$T_{t,h}$	510 K
Total temperature coolant	$T_{t,c}$	300 K
Turbulent length scale	l_ϵ	$0.73D$
Boundary layer displacement thickness	δ_1	$0.05D$

oblique viewing angle $\theta \approx 45°$.

Hot gas and coolant channel are seeded using silicon oil particles with a mean diameter of $d = 1\,\mu m$. Double images are acquired at a frequency of $f = 2\,kHz$ in frame-straddling mode with a time delay of $\Delta t = 10\,\mu s$ at multiple lateral y/D positions. For camera and laser synchronisation, a synchroniser by iLA5150 GmbH is used. A multi-pass scheme with an overlap of 50 % and a final interrogation window size of 16 px was used for data evaluation with PIVview3C by PIVTEC GmbH, yielding nearly two velocity vectors per millimetre.

The investigated film cooling hole geometry (Figure 2) constitutes a 10°-10°-10° laidback fan-shaped (LFH) hole with a cylindrical inlet segment. Compared to a real engine, it is scaled up by a factor of ≈ 14, yielding a diameter of the cylindrical part of the coolant hole of $D = 10\,mm$ to facilitate a high spatial measurement resolution. The length-to-diameter ratio is $L/D = 7.5$, the area ratio is $AR = A_{outlet}/A_{inlet} = 3.71$, and the coverage ratio (hole breakout width based on the pitch) is 0.35. The inlet and breakout edges of the diffuser are sharp-edged while the edges of the diffuser are rounded with $r_{edge} = 0.5D$. The pitch-to-diameter ratio is $p/D = 8$ with a total of five film cooling hole geometries each having an inclination angle of 35°.

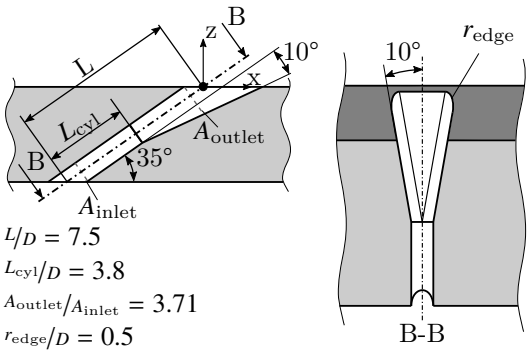

Figure 2: Film cooling hole geometry: 10°-10°-10° laidback fan-shaped hole; [8]

2.2 Measurement uncertainties

The measurement uncertainties associated with the flow parameters for both hot gas and coolant channel are detailed in [7]. Based on [14], the measurement uncertainty is below 12 % for the heat transfer coefficient with film cooling h_f in all regions where the adiabatic cooling effectiveness $\eta_{a,W} \leq 0.7$. The uncertainty for the adiabatic film cooling effectiveness $\eta_{a,W}$ is globally ≤ 0.012.

For the measurement uncertainty of PIV measurements, no globally accepted method is available. For this work, the uncertainties were estimated based on the correlation statistics method in [27]. In terms of absolute velocity, the spatially averaged relative local uncertainty was below 2.2 %. Everywhere except for the near-wall region, the local relative uncertainty was found to be below 5 %. Close to the wall for $y/D < 0.4$, the relative uncertainty increased locally towards the wall reaching up to 10 %. In streamwise direction, a slight decrease in uncertainty of less than 1 % was found.

3.0 AEROTHERMAL ANALYSIS

In the following sections, the flow field and the thermal film cooling parameters, such as film cooling effectiveness $\eta_{a,W}$ and ratio of heat transfer coefficients h_f/h_0, will be discussed for the blowing ratios $BR = 1.0,\ 2.0$ and 3.0. The overlap in streamwise direction between flow field measurements and thermal film cooling parameters is about $3.5D$.

3.1 Mean flow field analysis

The flow fields for all blowing ratios are given in Figure 3 for the central plane at $y/D = 0$ (Figure 3a) and for a lateral plane at $y/D = 1$ (Figure 3b). Each subfigure contains a contour of the absolute velocity u_{abs}, the wall normal component w and the lateral velocity v. Abrupt deviations in velocity compared to the surrounding values near the wall at $x/D \approx -0.9$ are due to reflections of the laser light sheet and resulting errors in PIV data processing.

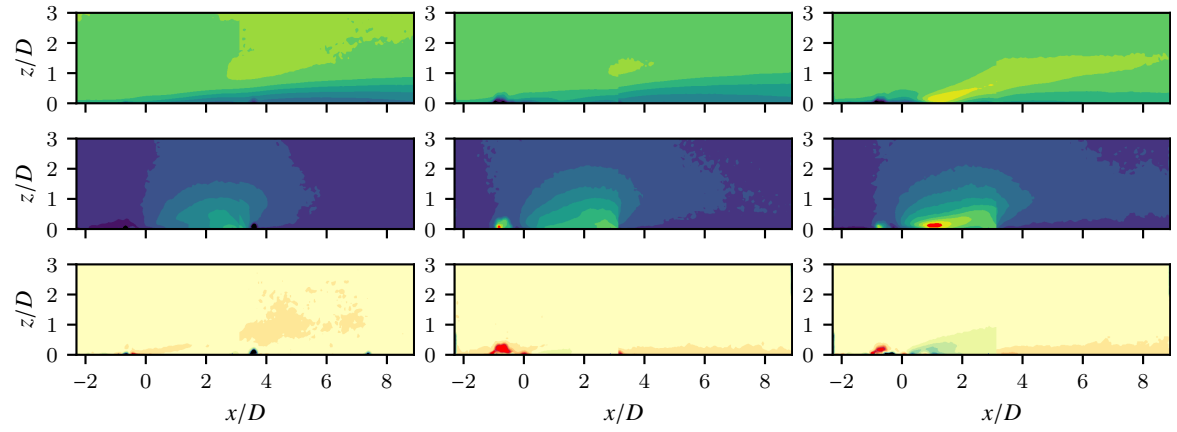

(a) $y/D = 0$, $BR = 1.0$, 2.0 and 3.0 (from left to right)

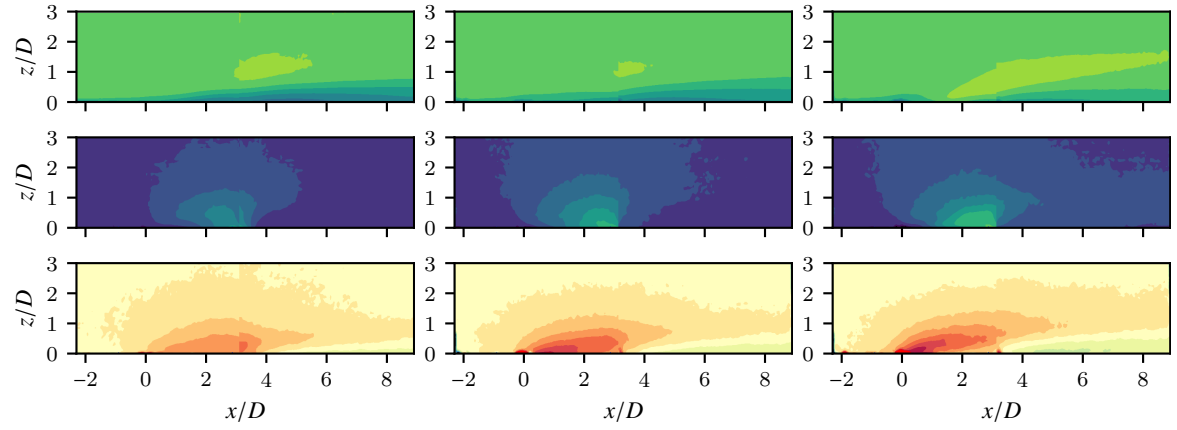

(b) $y/D = 1$, $BR = 1.0$, 2.0 and 3.0 (from left to right)

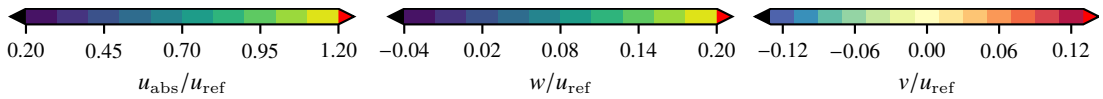

Figure 3: Normalised velocity fields for blowing ratios $BR = 1.0$, 2.0 and 3.0 for $y/D = 0$ and 1. Each subfigure contains (from top to bottom): u_{abs}, w and v

In Figure 4a, b and c, the velocities (u_{abs}, w and v, respectively) along the wall-normal direction at streamwise positions $x/D = 0$, 3 and 6 are given for the same two planes $y/D = 0$ and 1.

In Figure 3, it can be observed for both y/D positions and $BR = 1.0$ and 2.0 that due to the coolant ejection, the absolute velocity u_{abs} is significantly reduced compared to the hot gas main stream velocity u_{ref}. For the highest blowing ratio $BR = 3$ the average velocity at which the coolant is ejected is locally increased compared to the hot gas main stream velocity. This can be seen clearly also in Figure 4a at $x/D = 3$. This velocity peak decays quickly and is nearly not visible any more at $x/D = 6$.

For the central plane at $y/D = 0$, the peak in wall-normal velocity w shifts upstream with increasing blowing ratios (Figure 3a). For small blowing ratios, the main flow 'covers' the hole exit up to a certain x/D position leading to a coolant ejection biased towards the leeward side of the film cooling hole. While this effect might reduce or vanish completely for very high blowing ratios in cylindrical jet in crossflow (JICF) scenarios [1], it does not entirely vanish for the investigated laidback fan-shaped geometry. Even for $BR = 3.0$, the highest absolute velocities are found downstream of $x/D = 0$. In general, the wall-normal velocity component is much higher on the central plane at $y/D = 0$ compared to $y/D = 1$. For $x/D = 0$ and $y/D = 1$ (Figure 4b), negative wall-normal velocities can be observed in the near-wall region, suggesting hot gas ingestion into the coolant hole exit for $BR = 2.0$ and 3.0. At $x/D = 6$, no wall-normal component remains for any of the cases.

The lateral velocity component v at the central plane $y/D = 0$ is ≈ 0 for $BR = 1.0$, but deviates slightly

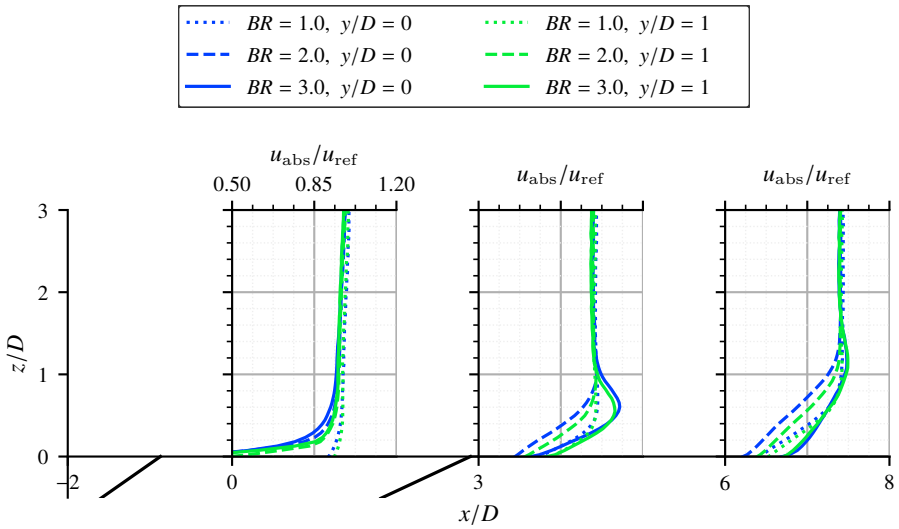

(a) Normalised velocity magnitude u_{abs} for $x/D = 0,\ 3$ and 6

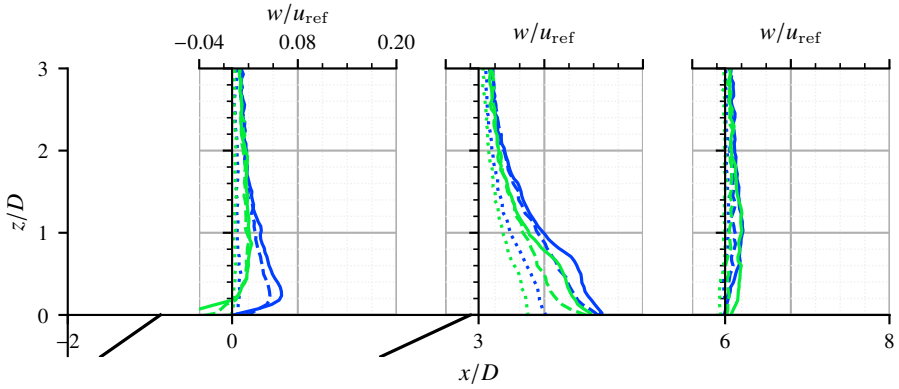

(b) Normalised wall-normal velocity w for $x/D = 0,\ 3$ and 6

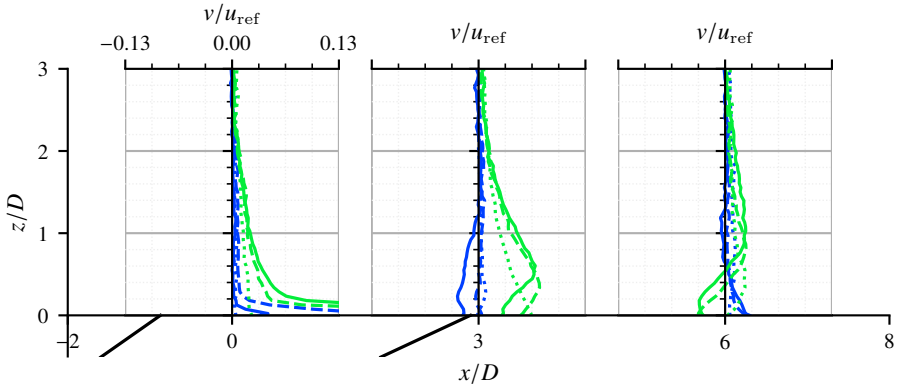

(c) Normalised lateral velocity v for $x/D = 0,\ 3$ and 6

Figure 4: Normalised absolute, wall-normal and lateral velocities along wall normal direction for multiple x/D positions. Solid black lines below the x-axes indicate the film cooling hole exit.

from zero for $BR = 2.0$ and 3.0, indicating a slight asymmetry for these blowing ratios. At $y/D = 1$, significant lateral velocity components v can be observed for all blowing ratios. Directly at the cooling hole exit, positive lateral velocities at a positive lateral position indicate the spreading of the coolant following the lateral expansion of the laidback fan-shaped cooling hole. The x/D position of the peak lateral velocity shifts upstream with increasing blowing ratios (Figure 3) while the z/D position of the

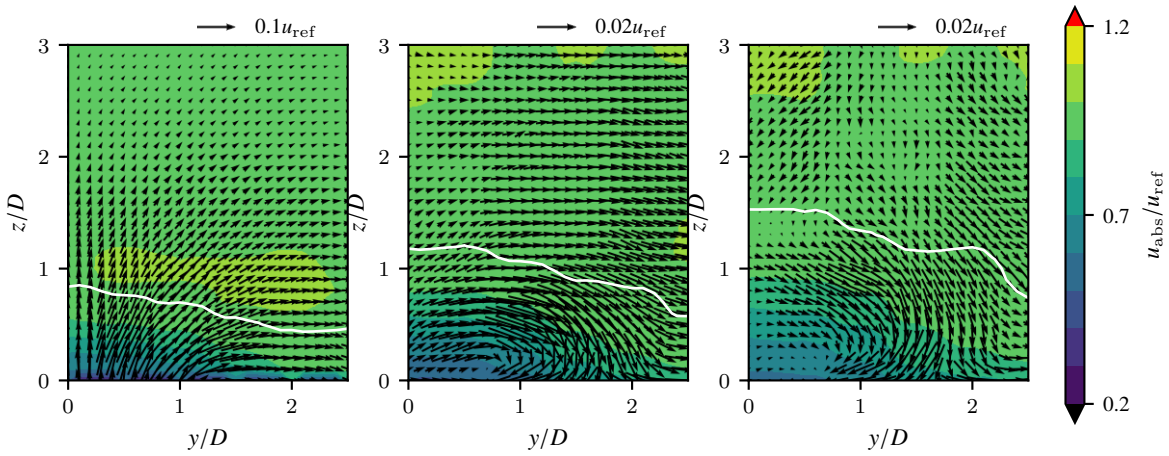

(a) $x/D = 3$ (b) $x/D = 6$ (c) $x/D = 8.5$

Figure 5: Velocity fields in the y, z-plane for $BR = 1.0$ for multiple x/D positions; white line indicates $u_{abs}/u_{ref} = 1$

peak shifts away from the wall as can be seen clearly in Figure 4c at $x/D = 3$. Downstream of the film cooling hole exit, an opposite, negative lateral velocity can be seen with an increase in magnitude and a shift in upstream direction with increasing blowing ratio. This indicates the counter-rotating vortex pair (CVP) which increases in strength with increasing blowing ratio.

The formation process of the CVP can be observed in Figure 5 for $BR = 1.0$ in the $y - z$-plane. The measurement data of multiple lateral measurement planes recorded for $0 \leq y/D \leq 2.5$ is interpolated onto a regular grid. The complete pitch is therefore not covered, but the formation of the CVP takes place in the presented coordinate range. The background contour constitutes the normalised absolute velocity and the vectors represent the in-plane velocity components v and w. A reference vector placed at the top right indicates the variable correspondence between vector length and velocity for each figure. At $x/D = 3$, the in-plane velocities are dominated by the wall-normal component w in the centre but the spreading in lateral direction due to the lateral expansion of the fan-shape cooling hole is clearly visible, deflecting the in-plane components in purely lateral direction towards $y/D = 2.5$. At $x/D = 3$ and $x/D = 6$, the left leg of the CVP is clearly visible and its distance to the wall increases slightly towards $x/D = 8.5$. As can be seen in Figure 3b, the strength of this vortex pair increases with increasing blowing ratio and so does the distance of the vortex legs to the wall as more hot gas main stream is entrained below the jet.

3.2 Adiabatic film cooling effectiveness and heat transfer

The thermal film cooling parameters for the investigated geometry were previously analysed [8] but from a purely thermal perspective. In Figure 6, the adiabatic film cooling effectiveness $\eta_{a,W}$ is presented for all three blowing ratios. The laterally averaged values of $\eta_{a,W}$ and of the ratio of heat transfer coefficients with and without film cooling h_f/h_0 are presented in Figure 7a and Figure 7b.

From Figure 6, it can be seen that $\eta_{a,W}$ increases strongly from $BR = 1.0$ to 2.0 but much less so from $BR = 2.0$ to 3.0. The lateral spreading reduces slightly for the highest blowing ratio and, as seen in Figure 7a, the laterally averaged adiabatic film cooling effectiveness $\bar{\eta}_{a,W}$ is even slightly reduced directly downstream of the coolant hole exit. Even further downstream, crossing $x/D \approx 13$, the highest blowing ratio exceeds $BR = 2.0$ in terms of $\bar{\eta}_{a,W}$. From the lateral distribution of the adiabatic film cooling effectiveness at $x/D = 6$ (Figure 8a) and the streamwise averaged lateral distribution $\bar{\eta}_{a,W,\bar{x}}$ (Figure 8b) it is evident that the highest blowing ratio does not recover from the lateral constriction. At $x/D = 6$, the lateral distribution of $\eta_{a,W}$ is nearly identical for $BR = 2.0$ and 3.0. The width of the lateral distribution is just slightly wider and the peak is very slightly larger for $BR = 2.0$. When averaged in streamwise direction within $5 \leq x/D \leq 50$, the lateral distribution of $\bar{\eta}_{a,W,\bar{x}}$ is still slightly wider for $BR = 2.0$ but the peak $\bar{\eta}_{a,W,\bar{x}}$ for $BR = 3.0$ is moderately higher. The increased laterally averaged adiabatic film cooling effectiveness $\bar{\eta}_{a,W}$ downstream of $x/D \approx 13$ in Figure 7a can therefore be attributed mainly to a higher film cooling effectiveness in the range of $-0.8 \leq y/D \leq 0.8$ for $BR = 3.0$.

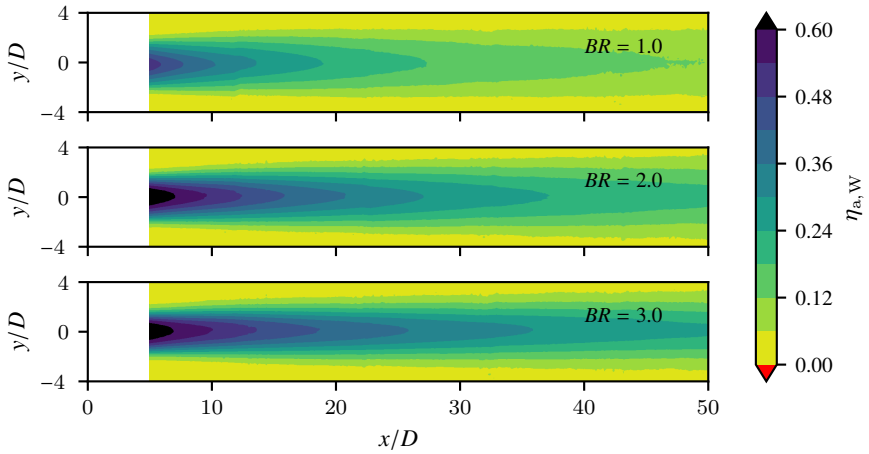

Figure 6: Adiabatic film cooling effectiveness downstream of coolant ejection for $BR = 1.0,\ 2.0$ and 3.0, [8]

3.3 Stationary and non-stationary vortex structures in film cooling

The four main vortical structures or categories of vortical structures that are typically associated with jets or transverse jets in crossflow are the counter-rotating vortex pair (CVP) (frequently also referred to as kidney vortex), a system of horseshoe vortices, a variety of shear layer vortices and wake vortices. Two of these, the shear layer vortices and the wake vortices, are inherently transient and cannot be identified in mean flow fields. The other two, the CVP and a system of horseshoe vortices, do have a mean flow definition but also unsteady components may be present, which cannot be identified in a mean flow analysis. [9, 13]

As shown in Figure 5 and Figure 3b, the stationary part of the CVP was identified clearly and increases in significance with increasing blowing ratio. The CVP is frequently associated with an adverse effect on cooling performance and a major portion of geometry optimisations in film cooling are directed towards impeding the CVP at the cooling hole exit. Its exact contributions to a decrease in adiabatic film cooling effectiveness $\eta_{a,W}$ or an increase in heat transfer coefficient are not entirely understood, since the majority of film cooling studies is focused on the thermal film cooling parameters only (an overview can be found in [4]). Also, studies exclusively focus on the impact of the mean flow representation of the CVP and neglect non-stationary contributions entirely.

To the knowledge of the authors, the second vortex structure possessing a mean flow definition, the horseshoe vortex, has not been detected experimentally in any investigations with operating parameters remotely relevant to film cooling. An increased turbulence intensity around the upstream edge of the exit of a cylindrical cooling hole was interpreted as proof for the presence of a horseshoe vortex by [28], while there is no trace of such flow structure in the presented velocity fields. Given the spatial resolution

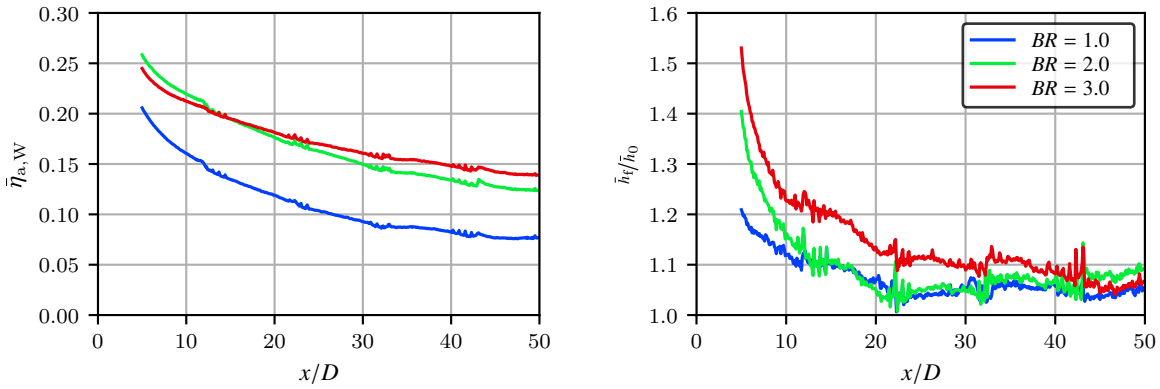

(a) $\bar{\eta}_{a,W}$ (b) $\bar{h}_f/\bar{h}_0$

Figure 7: Lateral averages of $\eta_{a,W}$ and h_f/h_0, [8]

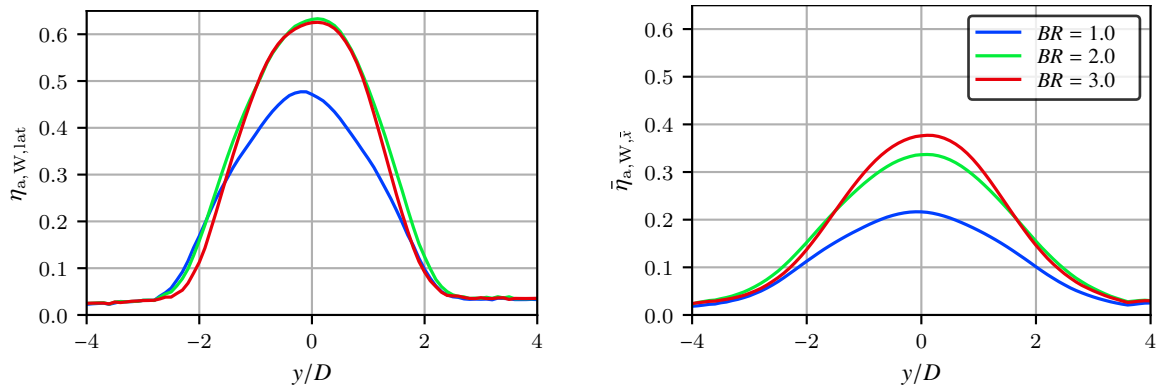

(a) $\eta_{a,W}$ at $x/D = 6$ (b) $\bar{\eta}_{a,W,\bar{x}}$ for $5 \leq x/D \leq 50$

Figure 8: Lateral distribution of $\eta_{a,W}$ at $x/D = 6$ and streamwise averaged adiabatic film cooling effectiveness $\bar{\eta}_{a,W,\bar{x}}$, [8]

of their measurement ($\approx 0.15D$) and the fact that only the cooling air was seeded, it is unlikely that the horseshoe vortex could have been detected in their setup. Despite the relatively high spatial resolution of the present study ($\approx 0.06D$) and a proper seeding of the entire flow field, no horseshoe vortex was detected for any of the blowing ratios. Considering the realistic turbulence intensity of the present study, the hole geometry and the position of the peak absolute velocities for different blowing ratios (see Figure 3), the horseshoe vortex might not exist at all or is extremely small and gets consumed quickly by the CVP [1]. In numerical studies using LES, [11] investigated cylindrical holes at orthogonal and inclined injection and did not identify horseshoe vortices. [30] investigated a laidback fan-shaped geometry using LES and found minor indications for a 'horseshoe-like' structure using the Q-criterion for visualisation of vortical structures.

To identify purely non-stationary vortex structures in the flow field, the proper orthogonal decomposition (POD), more specifically the snapshot POD, was applied to the fluctuating part of the 2D3C SPIV data. The POD identifies an orthonormal basis, the principal axes (or POD modes), while maximizing the variance within the data along these axes. These axes are calculated by solving an eigenvalue problem on the covariance matrix of the flattened velocity field time series. In the context of fluid dynamics, the resulting spatial POD modes are usually associated with coherent structures in the flow, while the time coefficients (temporal POD modes) describe the temporal evolution of the respective spatial mode [15]. The eigenvalues rank the POD modes according to the kinetic energy contained in the velocity fluctuations. The velocity field can be reconstructed using single modes or any arbitrary combination or amount of modes by multiplying each spatial mode with its time coefficient and adding

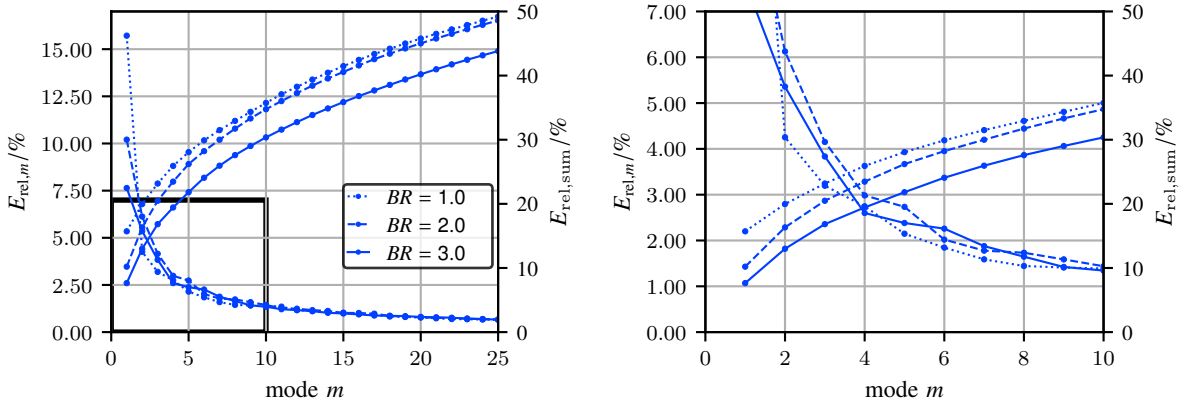

(a) (b)

Figure 9: Relative and cumulative relative energy ($E_{rel,m}$ and $E_{rel,sum}$) of POD spatial modes at $y/D = 0$, where b corresponds to the rectangular section in a marked by thick black lines

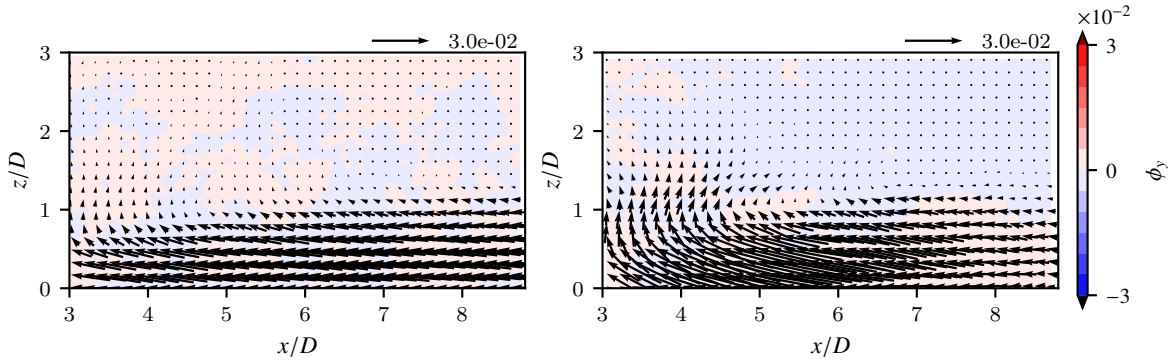

Figure 10: Fluctuation of coolant ejection: POD mode 1 for BR = 1.0 and 3.0 at y/D = 0

up the result of as many modes as intended. The sign associated with the spatial modes is ambiguous in the sense that it depends on the value of the time coefficient, which may be positive or negative and on average is zero. The POD modes, therefore, always have to be interpreted in conjunction with the mean flow field and the modulation it experiences due to a certain mode.

Since the measurement data was acquired using two separate FOVs, the POD cannot be conducted for the entire flow field at once as visualised in Figure 3, but separately for each time series. In the following, the POD results for the FOV, which lies immediately downstream of the cooling hole exit ($3 \lesssim x/D \lesssim 8.5$), will be analysed with focus on the central plane at $y/D = 0$.

In Figure 9, the kinetic energy of the first 25 POD modes is shown. The left axis indicates the relative kinetic energy of the velocity fluctuations in a certain mode, while the right axis specifies cumulative kinetic energy. For BR = 1.0 and 2.0, approximately 27 modes are required to recover 50 % of the kinetic energy of velocity fluctuations. For BR = 3.0, approximately 35 modes are required. The main difference lies with the first POD mode which is by definition associated with the largest relative kinetic energy. For BR = 1.0, 2.0 and 3.0, the first mode carries ≈ 16 %, 10 % and 7.5 %.

In Figure 10, the first spatial mode of BR = 1.0 and 3.0 can be seen. The in-plane components of the spatial modes are represented by the vectors and the out-of-plane component by the background contour. A reference vector indicates the correspondence between vector length and velocity magnitude at the top right of each figure.

For all blowing ratios, the first POD mode has negligible out-of-plane components. The in-plane components can be interpreted as the fluctuation of the coolant ejection. Due to the turbulence in the hot gas main flow and probable non-stationary flow separations in the cooling hole, the effective cross section of the cooling hole is a function of the instantaneous flow situation. The sections of the flow field that show significant in-plane components of the spatial mode are in the region nearer to the wall. In conjunction with the mean flow field, the first mode will increase or decrease, depending on the time coefficient, the near-wall streamwise velocities over the time series. The fraction of kinetic energy of

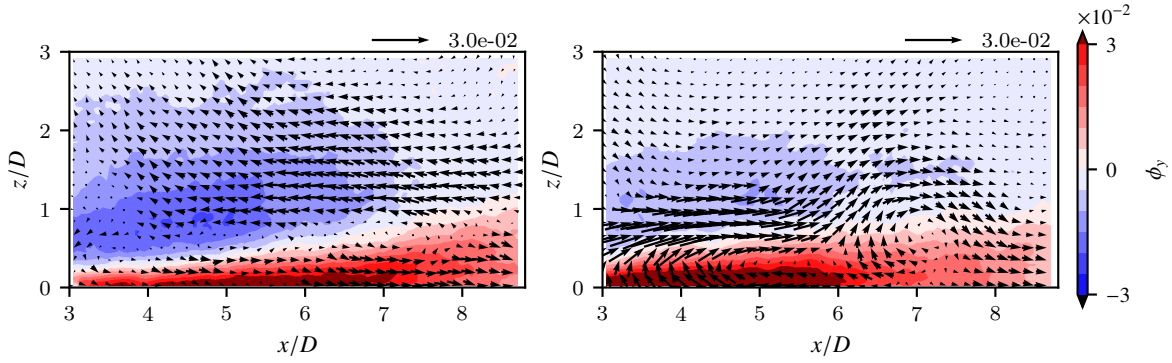

(a) POD mode 6 for BR = 2.0 (a) POD mode 5 for BR = 3.0

Figure 11: Non-stationary component of CVP: POD mode 6 for BR = 2.0 and POD mode 5 for BR = 3.0 at y/D = 0

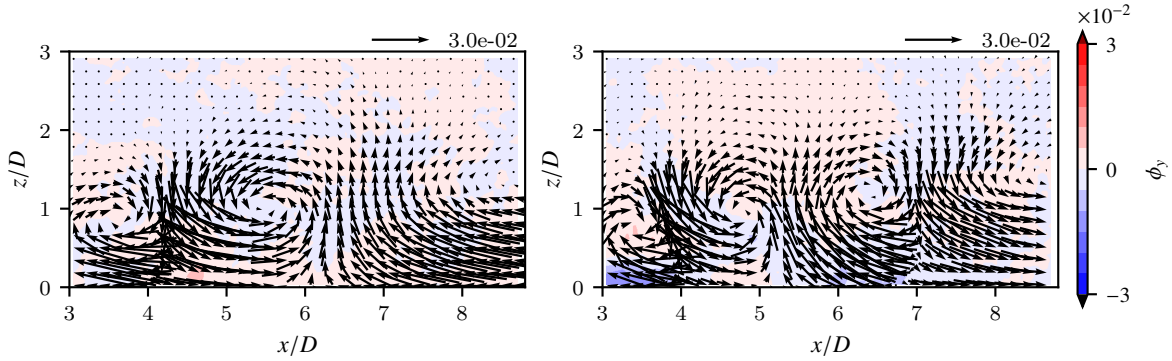

(b) POD mode 3 for $BR = 3.0$ (a) POD mode 4 for $BR = 3.0$

Figure 12: Shear layer vortices: POD mode 3 for $BR = 3.0$ and POD mode 4 for $BR = 3.0$ at $y/D = 0$

velocity fluctuations contained in this mode for $BR = 1.0$ is largest, as the smallest blowing ratio is affected by fluctuations in the main stream the most. With increasing blowing ratio, the significance of this mode decreases due to the larger coolant mass flow. The first mode of $BR = 2$ describes the same phenomenon and has the same basic structure as POD mode 1 for $BR = 1.0$ and 2.0.

Aside from the fluctuation of the coolant ejection itself, two more distinct structures will be discussed in the following. As mentioned earlier, even the stationary vortex structures may have contributions which fluctuate in time. For $BR = 2.0$ and 3.0, each two POD modes were identified in connection with the CVP and its non-stationary component. In Figure 11, POD mode 6 for $BR = 2.0$ and POD mode 5 for $BR = 3.0$ at $y/D = 0$ are displayed. In both cases, a strong out-of-plane component with somewhat horizontally layered opposite contributions can be observed. When compared to the mean flow field at $y/D = 1$, the similarity in shape, location and angle between the positive and negative zones becomes obvious. Since this mode was found at $y/D = 0$, it not only indicates a non-stationary component of the CVP, but also suggests a fluctuating lateral shift of the CVP.

Two spatial POD modes with similar appearance but shift in a certain direction illustrate the convection of a vortical structure in the specified direction [26]. Such behaviour can be observed in the present study and the modes are most likely related to shear layer instabilities in the upper shear layer of the coolant jet. In Figure 12, two such modes (POD modes 3 and 4) are shown for blowing ratio $BR = 3.0$. They are qualitatively similar but seem to be shifted in x-direction, which is the direction in which the shear layer of the film cooling jet should mainly be convected once the jet is bent in crossflow direction entirely. Similar modes indicating shear layer instabilities were found for $BR = 1.0$ and 2.0. The size and exact location of the vortical structures change for different blowing ratios and modes.

The last major non-stationary vortex structures usually associated with jets in cross-flow are the wake vortices. According to [20], wake vortices are roughly oriented in the same direction as the jet. In the present study, multiple modes potentially associated with wake vortices were found, some of them appearing in pairs with a shift in streamwise direction similar to that in the shear layer vortices. In

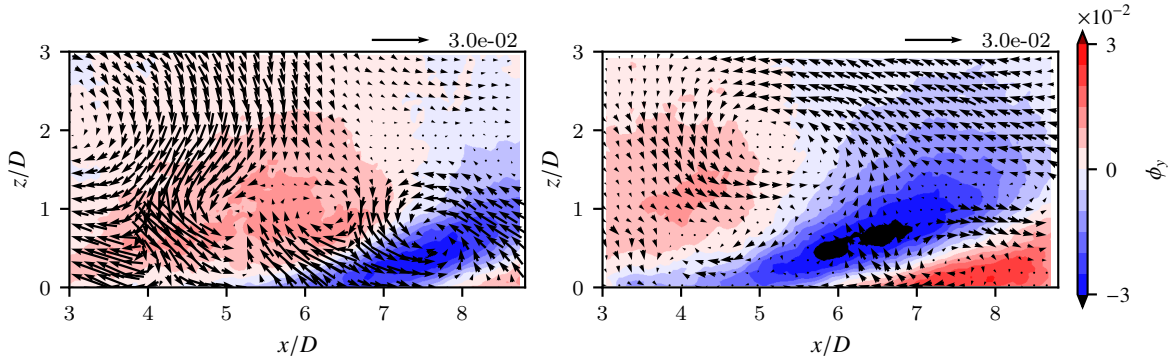

(b) POD mode 8 for $BR = 1.0$ (a) POD mode 10 for $BR = 2.0$

Figure 13: Wake vortices: POD mode 8 for $BR = 1.0$ and POD mode 10 for $BR = 2.0$ at $y/D = 0$

Figure 13, two different wake vortex modes are shown, one for $BR = 1.0$ and another for $BR = 2.0$. While these wake vortex modes appear for all blowing ratios, the amount of modes related to the wake vortices varies strongly depending on the blowing ratio. In the present study, they tend to appear earlier for lower blowing ratios and in general vary strongly in their spatial extent. In all cases and for all blowing ratios, the axes of the wake vortices are parallel within ±5° to the cooling hole axis with an inclination angle of ≈ 35°.

4.0 CONCLUSION AND OUTLOOK

In the present work, an attempt at combining flow field and thermal data and giving further insights into stationary and non-stationary vortex structures for jets in cross-flow in film cooling applications at realistic operating conditions was made for a 10°-10°-10° laidback fan-shaped film cooling hole geometry. Mean flow fields and thermal film cooling parameters were presented. For all blowing ratios, a fluctuation of the coolant ejection was found that is thought to be caused by fluctuations in the hot gas due to the realistic turbulence level as well as due to flow separations in the film cooling hole. Besides the well-known and frequently reported stationary component of the counter-rotating vortex pair (CVP), non-stationary components of the CVP were identified indicating a lateral fluctuation of the CVP position. Furthermore, purely non-stationary vortex structures, namely shear layer vortices and wake vortices were identified using POD. Both contain mode pairs with a characteristic shift indicating their convection in streamwise direction. The alignment of the wake vortices with the initial jet direction was confirmed.

For future research in jets in crossflow for film cooling applications, the vortical structures mainly responsible for increasing the heat transfer coefficient, causing the mixing between coolant and hot gas main stream reducing the cooling potential of the jet and reducing the film cooling effectiveness should be identified. Furthermore, the purely aerodynamic aspects like aerodynamic losses and influence of coolant ejection on the main flow stability should be analysed for discrete film cooling holes. Studies with focus on jets in cross-flow in combination with heat transfer are, however, currently relatively rare. Besides providing further understanding of this canonical flow field, further research in this area would also allow for more tailored solutions in all applications of jets in cross-flow where heat transfer is relevant. Furthermore, such data constitutes an excellent baseline for validation and further improvement of numerical methods.

ACKNOWLEDGEMENTS

The investigations were conducted as part of the joint research program COOREFLEX-turbo in the framework of AG Turbo. The work was supported by the Bundesministerium für Wirtschaft und Energie (BMWi) as per resolution of the German Federal Parliament under grant number 03ET7091O. The authors gratefully acknowledge AG Turbo and Siemens Energy AG for the support.

References

[1] Andreopoulos, J. and Rodi, W. [1984], 'Experimental investigation of jets in a crossflow', Journal of Fluid Mechanics 138, 93–127.

[2] Bernsdorf, S., Rose, M. G. and Abhari, R. S. [2005], 'Modeling of film cooling—part i: Experimental study of flow structure', Journal of Turbomachinery 128(1), 141–149.

[3] Bianchini, C., Andrei, L., Andreini, A. and Facchini, B. [2013], 'Numerical benchmark of non-conventional RANS turbulence models for film and effusion cooling', Journal of Turbomachinery 135(4).

[4] Bogard, D. G. and Thole, K. A. [2006], 'Gas turbine film cooling', Journal of Propulsion and Power 22(2), 249–270.

[5] Choe, H., Kays, W. and Moffat, R. [1974], The superposition approach to film-cooling, in 'American Society of Mechanical Engineers, Winter Annual Meeting'.

[6] Eberly, M. K. and Thole, K. A. [2013], 'Time-resolved film-cooling flows at high and low density ratios', Journal of Turbomachinery 136(6).

[7] Fraas, M., Glasenapp, T., Schulz, A. and Bauer, H.-J. [2017], Introducing a new test rig for

film cooling measurements with realistic hole inflow conditions, in 'Volume 5C: Heat Transfer', American Society of Mechanical Engineers.

[8] Fraas, M., Glasenapp, T., Schulz, A. and Bauer, H.-J. [2019], 'Film cooling measurements for a laidback fan-shaped hole: Effect of coolant crossflow on cooling effectiveness and heat transfer', Journal of Turbomachinery 141(4).

[9] Fric, T. F. and Roshko, A. [1994], 'Vortical structure in the wake of a transverse jet', Journal of Fluid Mechanics 279, 1–47.

[10] Gogineni, S., Pestian, D., Rivir, R. and Goss, L. [1996], PIV measurements of flat plate film cooling flows with high free stream turbulence, in '34th Aerospace Sciences Meeting and Exhibit', American Institute of Aeronautics and Astronautics.

[11] Guo, X., Schröder, W. and Meinke, M. [2006], 'Large-eddy simulations of film cooling flows', Computers & Fluids 35(6), 587–606.

[12] Johnson, B., Tian, W., Zhang, K. and Hu, H. [2014], 'An experimental study of density ratio effects on the film cooling injection from discrete holes by using PIV and PSP techniques', International Journal of Heat and Mass Transfer 76, 337–349.

[13] Karagozian, A. R. [2014], 'The jet in crossflow', Physics of Fluids 26(10), 101303.

[14] Kline, S. J. [1953], 'Describing uncertainty in single sample experiments', Mech. Engineering 75, 3–8.

[15] Kutz, J. N., Brunton, S. L., Brunton, B. W. and Proctor, J. L. [2016], Dynamic Mode Decomposition, Society for Industrial and Applied Mathematics.

[16] Margason, R. J. [1993], Fifty years of jet in cross flow research, Technical report, NASA Ames Research Center.

[17] Meyer, K. E., Pedersen, J. M. and Özcan, O. [2007], 'A turbulent jet in crossflow analysed with proper orthogonal decomposition', Journal of Fluid Mechanics 583, 199–227.

[18] Ochs, M., Horbach, T., Schulz, A., Koch, R. and Bauer, H.-J. [2009], 'A novel calibration method for an infrared thermography system applied to heat transfer experiments', Measurement Science and Technology 20(7), 075103.

[19] Ochs, M., Schulz, A. and Bauer, H.-J. [2010], 'High dynamic range infrared thermography by pixelwise radiometric self calibration', Infrared Physics & Technology 53(2), 112–119.

[20] Peterson, S. [2003], Structural features of jets-in-crossflow for film-cooling applications, in '41st Aerospace Sciences Meeting and Exhibit', American Institute of Aeronautics and Astronautics.

[21] Pietrzyk, J. R., Bogard, D. G. and Crawford, M. E. [1990], 'Effects of density ratio on the hydrodynamics of film cooling', Journal of Turbomachinery 112(3), 437–443.

[22] Roach, P. [1987], 'The generation of nearly isotropic turbulence by means of grids', International Journal of Heat and Fluid Flow 8(2), 82–92.

[23] Stichling, K., Elfner, M. and Bauer, H.-J. [2021], 'Investigation of film cooling using time-resolved stereo particle image velocimetry', Journal of Turbomachinery 143(7).

[24] Tucker, P. [2011], 'Computation of unsteady turbomachinery flows: Part 2—LES and hybrids', Progress in Aerospace Sciences 47(7), 546–569.

[25] Wang, C., Zhang, J., Feng, H. and Huang, Y. [2018], 'Large eddy simulation of film cooling flow from a fanshaped hole', Applied Thermal Engineering 129, 855–870.

[26] Weiss, J. [2019], A tutorial on the proper orthogonal decomposition, in 'AIAA Aviation 2019 Forum', American Institute of Aeronautics and Astronautics.

[27] Wieneke, B. [2015], 'PIV uncertainty quantification from correlation statistics', Measurement Science and Technology 26(7), 074002.

[28] Wright, L. M., McClain, S. T. and Clemenson, M. D. [2011a], 'Effect of freestream turbulence intensity on film cooling jet structure and surface effectiveness using PIV and PSP', Journal of Turbomachinery 133(4).

[29] Wright, L. M., McClain, S. T. and Clemenson, M. D. [2011b], PIV investigation of the effect of freestream turbulence intensity on film cooling from fanshaped holes, in 'Volume 5: Heat Transfer, Parts A and B', ASMEDC.

[30] Zamiri, A., You, S. J. and Chung, J. T. [2020], 'Large eddy simulation of unsteady turbulent flow

structures and film-cooling effectiveness in a laidback fan-shaped hole', Aerospace Science and Technology 100, 105793.